Electro-Optomechanical Modulation Instability in a Semiconductor Resonator

Pierre Etienne Allain,[1] Biswarup Guha,[1] Christophe Baker,[1] David Parrain,[1]
Aristide Lemaître,[2] Giuseppe Leo,[1] and Ivan Favero[1]
[1]*Matériaux et Phénomènes Quantiques, Université de Paris, CNRS UMR 7162, 10 rue Alice Domon et Léonie Duquet 75013 Paris, France*
[2]*Centre de Nanosciences et Nanotechnologies, CNRS UMR 9001, Université Paris-Saclay, 91120 Palaiseau, France*

(Received 9 December 2020; accepted 20 May 2021; published 17 June 2021)

In semiconductor nano-optomechanical resonators, several forms of light-matter interaction can enrich the canonical radiation pressure coupling of light and mechanical motion and give rise to new dynamical regimes. Here, we observe an electro-optomechanical modulation instability in a gallium arsenide disk resonator. The regime is evidenced by the concomitant formation of regular and dense combs in the radio-frequency and optical spectrums of the resonator associated with a permanent pulsatory dynamics of the mechanical motion and optical intensity. The mutual coupling between light, mechanical oscillations, carriers, and heat, notably through photothermal interactions, stabilizes an extended mechanical comb in the ultrahigh frequency range that can be controlled optically.

DOI: 10.1103/PhysRevLett.126.243901

Storing light in a small cavity for a long time can enhance light-matter interactions. The approach has been employed to study the quantum electrodynamics of atoms [1], to engineer efficient lasers [2], or to investigate nonlinear optical phenomena that emerge at large optical densities [3,4]. The richness of nonlinear optics is illustrated by various routes to chaos: under continuous-wave laser driving and for an increasing power, the linear single-frequency output of a system can be substituted by a multifrequency response, by the formation of temporal and spatial patterns such as solitary waves, or by a chaotic type of response where no apparent order surfaces [5]. A train of pulses usually precedes the emergence of optical solitons, a situation referred to as modulation instability [6,7], which has been observed in fibers, bulk crystals, semiconductor waveguide arrays, liquid crystals, and dielectric cavities [8–10].

Mechanically compliant optical cavities may also confine light in order to enhance interactions, this time with a mechanical degree of freedom that replaces the atom, the gain, or the nonlinear medium [11,12]. In high refractive index semiconductor optomechanical resonators, photons and phonons are colocalized in a submicron interaction volume, leading to large optomechanical couplings [13–15]. At this level of energy concentration, not only the optomechanical nonlinearity but other nonlinearities as well are expected to surge. In gallium arsenide (GaAs) disk resonators for example, a platform known for optomechanics [16,17], the second-order optical nonlinearity was recently used for frequency conversion in high-Q whispering gallery resonators [18–21]. In silicon photonic crystal resonators, the nonlinear optical absorption and thermo-optical response of the material were combined with optomechanical coupling in order to provide a route to chaos at large optical power [22,23], which differed from that observed in the case of a mere radiation pressure interaction [24]. Different regimes were observed in these experiments: optomechanical self-oscillations, self-induced optical modulation, generation of stable mechanical subharmonics in the optical output, and a fully developed chaos. Other permanent regimes may yet arise from the combination of various nonlinearities in a miniature optomechanical resonator, depending on the specific conditions met. This is the subject of the present Letter.

Here we report on the observation of a regime of electro-optomechanical modulation instability in a GaAs disk resonator. The regime is evidenced by the concomitant formation of regular and dense combs in the radio-frequency and optical spectrums of the resonator associated with a permanent pulsatory dynamics of the mechanical motion and optical intensity. A model, whose parameters have been carefully analyzed, quantitatively explains the emergence of this modulation instability and its evolution by the mutual couplings between the optical cavity field, the mechanical motion, and carriers and heat generated by linear and nonlinear optical absorption. The phenomenon settles at large optical power, beyond optomechanical self-oscillation, and enables the all-optical generation of a mechanical frequency comb in the ultrahigh frequency range. The latter is stable and reaches a spectral span of one tenth of the carrier frequency.

Our GaAs disks are positioned in line on a mesa structure elevated above the substrate, as shown in Fig. 1(a). This allows using a straight tapered fiber for evanescent coupling experiments [Fig. 1(b)], leading to a better control of polarization and mechanical stability compared to our past

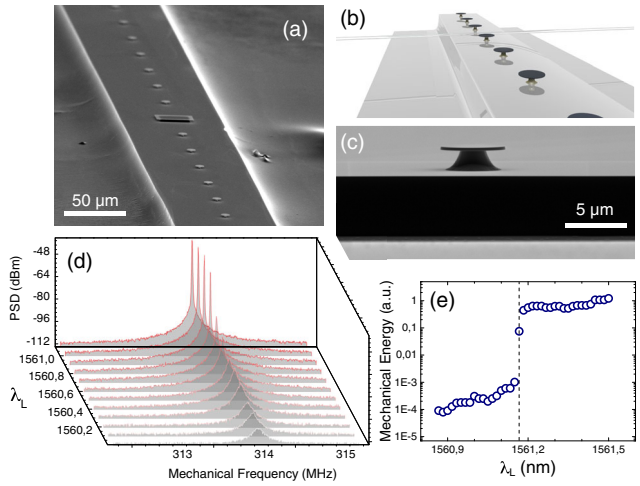

FIG. 1. GaAs disk optomechanical (self-)oscillators. (a) Electron micrograph of the mesa supporting a row of disk resonators. (b) Illustration of the straight fiber taper evanescently coupled to a disk of the row. (c) Side-view electron micrograph of a single disk. (d) Series of rf spectra showing the transition to optomechanical self-oscillation. (e) Threshold of the optomechanical self-oscillation regime as function of the driving wavelength.

looped fiber technique [14,16,25]. The disks have a radius between 2 and 5 μm and a thickness of 200 nm [Fig. 1(c)]. Resonators and mesa are fabricated out of an epitaxial GaAs/AlGaAs (aluminum gallium arsenide) heterostructure using a combination of electron-beam and optical lithography and three distinct wet-etch steps. The disks are optically pumped through the fiber taper by a continuous-wave tunable single-mode laser operating at the telecom wavelength, while light at the fiber output is collected on a GHz-bandwidth photodetector. Under evanescent coupling, the disk mechanical motion modulates the fiber transmission, whose radio-frequency noise spectrum is analyzed electronically at the output of the photodetector.

Figure 1(d) shows the evolution of the obtained radio-frequency noise spectrum at moderate optical power in the fiber ($\sim$50 μW), for a laser blue-detuned on the flank of a whispering gallery mode (WGM1) resonance of a disk of radius 4.5 μm as the laser wavelength is progressively increased to reduce the detuning (bottom to top curve). The bottom spectrum (white) displays a single peak at 314 MHz corresponding to the fundamental radial breathing mode of the disk driven by thermal fluctuations [16]. This peak is progressively narrowed and amplified before abruptly acquiring a large amplitude and a strongly reduced linewidth. In the time domain, this corresponds to the onset of quasisinusoidal mechanical motion sustained by optomechanical forces, a situation often referred to as optomechanical (self-)oscillation [26–29]. The oscillator transition and its threshold are better appreciated by plotting the area under the radio-frequency peak as a function of the driving laser wavelength [see Fig. 1(e)], which controls the detuning frequency and the number of intracavity photons, two key parameters of the amplification process [11,12]. In the specific case of the present GaAs disk operated at room temperature, the optomechanical self-oscillation is governed by a combination of radiation pressure, electrostriction, and photothermal interactions, as detailed by experiments and a model elsewhere [30]. The latter model will be completed below in order to explain the richer dynamics developing at larger drive power beyond optomechanical self-oscillation, which we now describe.

At larger power (typically $\geq$ 300 μW), the output light spectrum acquires a very regular comb pattern in the optical and radio-frequency domains. Figure 2(a) shows an example of the optical comb generated at the output of our GaAs disk resonator driven close to WGM1 resonance, measured with a high-resolution (5 MHz) optical analyzer, with teeth separated by the mechanical frequency at 314 MHz. Several tens of teeth are visible in the spectrum, appearing as sidebands extending over a few tenths of picometers around the optical carrier wavelength at 1569.397 nm. The formation of such an optical comb is a feature known to accompany optomechanical self-oscillation, as reported in early work on the subject [27]. Less usual, in contrast, is the comb forming in the radio-frequency domain, visible in Fig. 2(b). Stable and regular, it is centered around the mechanical frequency and consists of about 30 visible teeth, with a frequency separation slightly below the MHz in this example. The latter comb formation, together with its exact spectral structure, is elucidated below by

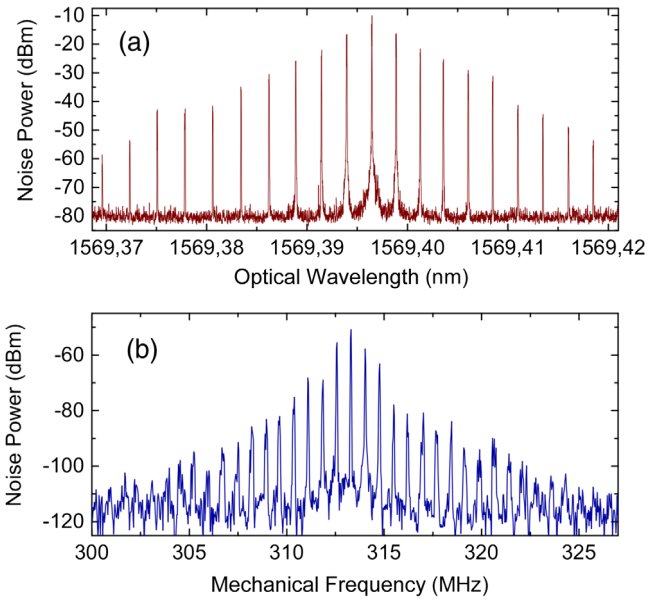

FIG. 2. Dual-comb structure in the electro-optomechanical modulation instability regime. (a) Optical spectrum of the light at the output of a GaAs disk resonator driven at large power. (b) Radio-frequency spectrum of the output light under the same conditions.

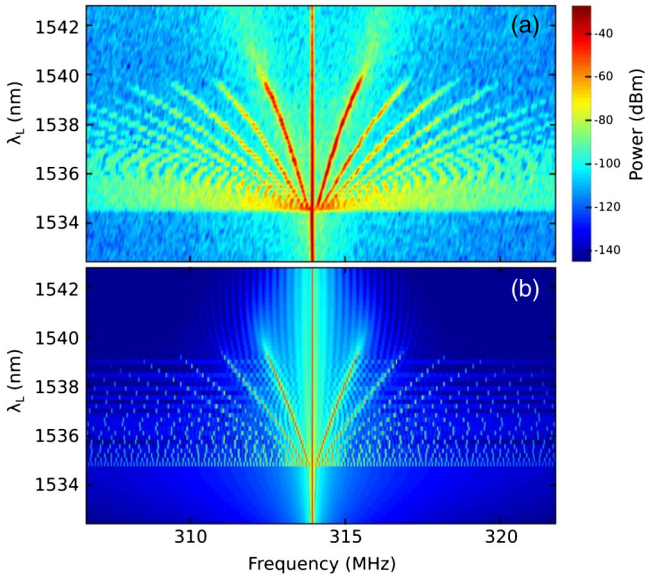

FIG. 3. Evolution of the electro-optomechanical modulation instability radio-frequency spectrum as function of the driving laser wavelength. (a) Experiment. (b) Theory.

investigating the phenomenon in detail as function of the optical pump wavelength and power.

Figure 3(a) follows the gradual evolution of a GaAs disk optomechanical resonator from the optomechanical self-oscillation regime to the double comb formation introduced above. The evolution is shown on a two-dimensional map of the output radio-frequency spectrum as function of the optical drive wavelength λ_L. The resonator of 4.5 μm radius is driven on the blue-detuned flank of a second WGM optical resonance in the vicinity of 1530 nm of wavelength (WGM2) with an optical power of 3.56 mW in the fiber taper, and the laser detuning is progressively reduced as λ_L is increased (bottom to top spectrum). λ_L serves here as the control parameter of the evolution, but the optical power can be employed as well (not shown). At the starting wavelength in this map ($\lambda_L \sim 1533$ nm), the spectrum consists of a single narrow line at 314 MHz corresponding to the self-sustained optomechanical oscillation regime. At $\lambda_L \sim 1534.3$ nm, the spectrum suddenly develops a noisy background extending over 20 MHz around the mechanical frequency. As λ_L is further increased, a very regular structure emerges from this background, with sidebands equally spaced and progressively incrementing in number. The frequency spacing between these teeth increases as λ_L further increases, rising above 1 MHz at $\lambda_L \sim 1540$ nm. Beyond this point, these regular sidebands progressively fade away, letting the self-oscillatory mechanical motion dominate the dynamics again, with a single narrow peak in the spectrum.

In order to elucidate this behavior, we build on the optomechanical model introduced in [30], which includes radiation pressure, electrostrictive, and photothermal interactions. We extend the model by adding several nonlinearities. The two-photon absorption (TPA) of telecom photons leads to the generation of heat and free carriers. The heat increases the resonator temperature, which affects the intracavity photons through the thermo-optic effect. Photons are concomitantly affected by free carriers through free-carrier dispersion (FCD) and absorption (FCA). The competition between these (slow) thermal and (fast) carrier nonlinearities is known to generate a rich radio-frequency dynamics in optical resonators [31]. Instead of the three coupled differential equations of [30] (optical, mechanical, thermal), we deal now with four coupled equations (optical, mechanical, thermal, free carriers). In contrast to [22,23], our model includes the photothermal interaction (also dubbed bolometric force), which is a central ingredient in room temperature optomechanics [29,30]: a mechanical displacement is generated by the thermal expansion following the absorption of photons, be it linear or nonlinear. The photothermal coupling transfers some of the thermal and optical dynamics to the mechanical degree of freedom, an important feature here. As shown below, this new model allows us to quantitatively reproduce the complex dynamics observed in our experiments. The four coupled equations read as follows:

$$\dot{a}(t) = -\frac{\kappa}{2}a(t) + i\left[\Delta^b\omega + g_{\mathrm{om}}x(t) + \frac{\omega_{\mathrm{cav}}}{n}\frac{dn}{dT}\Delta T(t) + \frac{\omega_{\mathrm{cav}}}{n}\frac{dn}{dN}N(t)\right]a(t) + \sqrt{\kappa_{\mathrm{ex}}}a_{\mathrm{in}}(t), \tag{1}$$

$$m_{\mathrm{eff}}[\ddot{x}(t) + \Gamma_m\dot{x}(t) + \omega_m^2 x(t)] = F_{\mathrm{opt}}(t) + F_{\mathrm{pth}}(t), \tag{2}$$

$$\dot{\Delta T}(t) = -\frac{\Delta T(t)}{\tau_{\mathrm{th}}} + \frac{R_{\mathrm{th}}\hbar\omega_L}{\tau_{\mathrm{th}}}(\kappa_{\mathrm{lin}} + \kappa_{\mathrm{TPA}} + \kappa_{\mathrm{FCA}})|a(t)|^2, \tag{3}$$

$$\dot{N}(t) = -\frac{N(t)}{\tau_{\mathrm{fc}}} + \frac{\beta_{\mathrm{TPA}}c^2\hbar\omega_L}{2n_g^2V_{\mathrm{FCA}}^2}|a(t)|^4. \tag{4}$$

Equation (1) governs the complex cavity optical field $a(t)$, normalized such that $|a(t)|^2$ is the number of cavity photons, κ is the total cavity energy decay rate, and κ_{ex} the external coupling rate to the optical input field a_{in}, normalized such that $|a_{\mathrm{in}}|^2 = P_L$ is the input laser power.

$\Delta^b\omega = \omega_L - \omega_{\mathrm{cav}}$ is the detuning of the laser frequency ($\omega_L = 2\pi c/\lambda_L$) to the bare cavity resonance frequency (ω_{cav}), $g_{\mathrm{om}} = -\partial\omega_{\mathrm{cav}}/\partial x$ the frequency-pull parameter, $x(t)$ the mechanical displacement, n a modal refractive index, dn/dT the associated thermo-optic coefficient, ΔT the increase in disk temperature, and dn/dN the free-carrier dispersion coefficient with N the density of free carriers. Equation (2) describes a mechanical harmonic oscillator of frequency ω_m, effective mass m_{eff}, and damping $\Gamma_m = \omega_m/\mathrm{Q_m}$, driven by conservative optical forces $F_{\mathrm{opt}} = F_{\mathrm{rp}} + F_{\mathrm{el}}$ (radiation pressure and electrostriction) summed with a dissipative photothermal force proportional to the temperature increase $F_{\mathrm{pth}} = \alpha\Delta T$. Equation (3) governs the thermal behavior of the resonator, with τ_{th} the thermal relaxation time and R_{th} the thermal resistance that links, at steady state, the temperature increase to the intracavity absorbed power $\Delta T = R_{\mathrm{th}}(\kappa_{\mathrm{lin}} + \kappa_{\mathrm{TPA}} + \kappa_{\mathrm{FCA}})\hbar\omega_L|a|^2$. The intracavity absorption rate is the sum of a linear (κ_{lin}), two-photon (κ_{TPA}), and free-carrier (κ_{FCA}) absorption rates, with $\kappa_{\mathrm{TPA}} = (\beta_{\mathrm{TPA}}c^2/V_{\mathrm{TPA}}n_g^2)\hbar\omega_L|a|^2$ and $\kappa_{\mathrm{FCA}} = (\sigma_{\mathrm{FCA}}c/n_g)N$, where β_{TPA} is the two-photon absorption coefficient (in m/W), n_g is the group-velocity index, $V_{\mathrm{TPA}} = [\int n^2(\mathbf{r})|E(\mathbf{r})|^2 d\mathbf{r}]^2/\int n^4(\mathbf{r})|E(\mathbf{r})|^4 d\mathbf{r}$ is the nonlinear volume, and σ_{FCA} is the FCA cross section [32]. The total loss rate $\kappa = \kappa_0 + \kappa_{\mathrm{ex}} + \kappa_{\mathrm{TPA}} + \kappa_{\mathrm{FCA}}$ now includes several channels, with $\kappa_0 = \kappa_{\mathrm{lin}} + \kappa_{\mathrm{rad}}$ the intrinsic decay rate of the cavity mode and κ_{rad} the radiative contribution. Equation (4) describes the evolution of the density N of free carriers generated by TPA. It involves the free-carrier relaxation time τ_{fc} and the FCA volume given by $V_{\mathrm{FCA}}^2 = [\int n^2(\mathbf{r})|E(\mathbf{r})|^2 d\mathbf{r}]^3/\int n^6(\mathbf{r})|E(\mathbf{r})|^6 d\mathbf{r}$ [32]. In the present work, where the whispering gallery mode is mostly confined within the semiconductor material, the confinement factors Γ_{TPA} and Γ_{FCA} [32] have been omitted for simplicity.

The above set of four equations is closed and involves multiple parameters, which can be all evaluated independently by measurements or calculations. κ_{ex} and κ_0 are measured through systematic evanescent coupling experiments with a varying gap [33]. $P_L, \Delta^b\omega, \Gamma_m, \omega_m$, and g_{om} are measured through linear optical and mechanical spectroscopy [16], the latter parameter being also consistently obtained by finite element method (FEM) simulations as the sum of a geometric ($g_{\mathrm{om}}^{\mathrm{geo}}$) and a photoelastic ($g_{\mathrm{om}}^{\mathrm{pe}}$) contribution [15]. $n, dn/dT, dn/dN, \beta_{\mathrm{TPA}}$ and σ_{FCA} are calculated for the considered mode, starting from tabulated values under the here-employed telecom wavelength and room temperature conditions. The conservative forces are obtained through $F_{\mathrm{rp}} = \hbar g_{\mathrm{om}}^{\mathrm{geo}}|a(t)|^2$ and $F_{\mathrm{el}} = \hbar g_{\mathrm{om}}^{\mathrm{pe}}|a(t)|^2$, while the α coefficient of the photothermal force is computed using Eqs. 3.9 and 3.13 of [34]. Knowing the disk pedestal properties, τ_{th} and R_{th} are computed by FEM, and we obtain consistently τ_{th} from a frequency response measurement [35] and the product $\kappa_{\mathrm{lin}} \times R_{\mathrm{th}}$ from a fit of the thermo-optic distortion of the WGM resonance at intermediate optical powers [30,36]. Finally, V_{TPA} and V_{FCA} can be computed by FEM, while τ_{fc} is measured by time-resolved photoluminescence [37].

TABLE I. Parameters.

Parameter	Value	Description
ω_{cav}	$2\pi \cdot 1.96 \times 10^{14}$ Hz	Bare cavity frequency
κ_0	$2\pi \cdot 1.25 \times 10^{10}$ Hz	Intrinsic cavity decay
κ_{ex}	$2\pi \cdot 1.61 \times 10^{9}$ Hz	Extrinsic cavity decay
P_L	3.56 mW	Input laser power
g_{om}	$2\pi \cdot 5.24 \times 10^{19}$ Hz.m^{-1}	Frequency-pull parameter
dn/dT	2.3×10^{-4} K^{-1}	Thermo-optic coefficient
dn/dN	-5.53×10^{-27} m^3	FCD coefficient
ω_m	$2\pi \cdot 314$ MHz	Mechanical frequency
m_{eff}	53 pg	Effective mass
Γ_m	$2\pi \cdot 1.01 \times 10^{5}$ Hz	Mechanical damping
α	1.9 μN.K^{-1}	Photothermal coefficient
τ_{th}	0.97 μs	Thermal relaxation time
R_{th}	3.78×10^{6} K.W^{-1}	Thermal resistance
κ_{lin}	$2\pi \cdot 4.14 \times 10^{7}$ Hz	Linear absorption rate
β_{TPA}	2.66×10^{-9} m.W^{-1}	TPA coefficient
n_g	2.6	Group velocity index
V_{TPA}	4.66×10^{-18} m^3	Nonlinear TPA volume
σ_{FCA}	6.03×10^{-21} m^2	FCA cross section
τ_{fc}	14 ps	Free-carrier relaxation time
V_{FCA}	4.57×10^{-18} m^3	FCA volume

This leaves the model with no adjustable parameter. In practice, when running the model to fit the data, we did, however, let κ_{lin}, R_{th}, τ_{th}, α, τ_{fc}, V_{TPA}, and V_{FCA} slightly vary around their first estimated value within our estimation precision window. Table I lists the eventually employed parameter values, which all fall within this window. The only parameter showing some deviation is β_{TPA}, a factor of 9 above the bulk value generally reported in the literature. This finding may be the result of the field confinement in our WGM resonators, which can modify the TPA by a few units [38], and of the presence of midgap states at the resonator surface [36,37], which can assist nonlinear absorption [39]. Figure 3(b) shows the result of the modeling procedure, where the radio-frequency spectrum of the optical transmission is displayed as a function of laser wavelength. The model satisfactorily reproduces the experimental spectral response and all its salient features: the onset point of the comb formation is correctly retrieved, as well as its vanishing point, and the number of teeth together with their spectral separation are also precisely reproduced as a function of laser wavelength.

The electro-optomechanical modulation instability regime, where the radio-frequency comb is fully developed and stabilized, can also be observed by looking at the time response of the system. Figure 4(a) shows the optical transmission calculated from the above model under the conditions of Fig. 3. On top of the expected modulation at

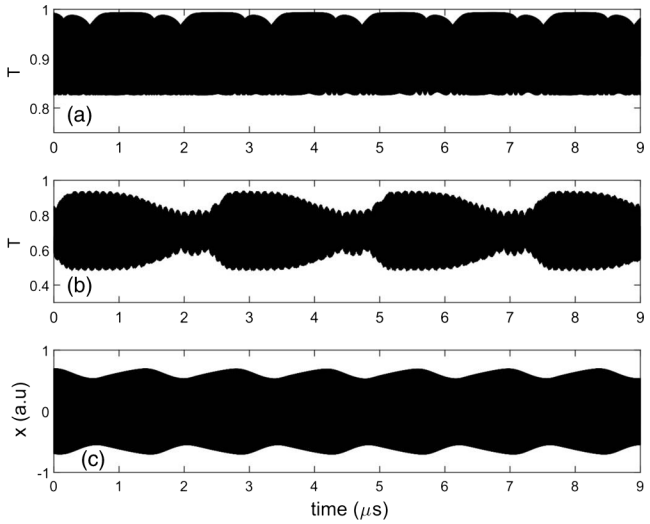

FIG. 4. Variety of the temporal dynamics met in the electro-optomechanical modulation instability regime. (a) Normalized transmission at the output of the fiber for WGM2, calculated from the model. (b) Time trace of the normalized transmission at the output of the fiber for WGM3, measured experimentally. (c) Mechanical displacement as function of time under same conditions as (a).

the mechanical frequency of 314 MHz (not visible at the scale of this plot), it displays a pronounced modulation of the envelope at fast (∼10 ns) and slow (∼1.5 and 0.5 μs) timescales. In order to appreciate the variety of the observed dynamics, we report in Fig. 4(b) an experimental time trace of the fiber taper transmission obtained on the same resonator using a distinct optical mode (WGM3), whose spatial profile and coupling to free carriers differ from those of WGM2. The time modulation is this time more symmetric and smoother, with a fast (slow) modulation time reaching ∼100 ns (2.5 μs). Interestingly, the temporal behavior of the mechanical displacement $x(t)$ in the modulation instability regime is also remarkably regular, as visible in the time trace of Fig. 4(c) calculated from the model under the conditions of Fig. 3. On top of the oscillation at 314 MHz (not visible at this scale), it displays a very stable pulsing of the envelope at a slow timescale of ∼1 μs. The latter time can be varied with operating conditions, acting for example on the detuning or on the input power. In this regime, the spectrum of the mechanical motion acquires an extended frequency comb structure, which is shown in the Supplemental Material [40].

In conclusion, we unravel here a new regular dynamical regime in optomechanical resonators, where carriers and heat interplay with canonical optomechanical coupling. Our experimental findings are precisely recovered using a model of four coupled equations, whose parameters have been carefully determined. The most remarkable experimental result is the stabilization of a dense and ordered rf comb around the mechanical carrier frequency, which manifests itself in the spectrum of the output light and in the dynamics of the mechanical motion. The latter acquires a very regular temporal behavior, where a smooth modulation of the envelope adds to the stable carrier frequency to generate a multifrequency mechanical clock. The question arises as to whether such a mechanical frequency comb [41–43] can be made stable enough to be employed in force sensing [35,44] with some advantage. Optomechanical magnetometers [45], atomic force [46–48], or mass sensors [49,50] may benefit from the development of mechanical comb spectroscopy controlled by light. Investigating these possibilities will require an in-depth analysis of noise mechanisms in the here-presented electro-optomechanical oscillators and will be the subject of future work.

This work was supported by the European Research Council via the GANOMS (306664) and NOMLI (770933) projects and by the Agence Nationale de la Recherche through the Quantera QuaSeRT and Olympia projects.

[1] S. Haroche and J. M. Raimond, *Exploring the Quantum* (Oxford University Press, Oxford, England, 2006).
[2] A. E. Siegman, *Lasers* (Oxford University Press, Oxford, England, 1986).
[3] N. W. Bloembergen, *Nonlinear Optics* (W. A. Benjamin, New York, 1965).
[4] R. W. Boyd, *Nonlinear Optics* (Academic Press, Orlando, 2008).
[5] P. Bergé, Y. Pomeau, and C. Vidal, *L'ordre dans le Chaos* (Hermann, Paris, 1997).
[6] S. Wabnitz, Phys. Rev. A **38**, 2018 (1988).
[7] B. Daino, G. Gregori, and S. Wabnitz, J. Appl. Phys. **58**, 4512 (1985).
[8] G. Agrawal, *Nonlinear Fiber Optics* (Academic Press, Cambridge, 1995).
[9] *Spatial Solitons*, edited by S. Trillo and W. Torruellas (Springer Series in Optical Sciences, New York, 2001).
[10] S. Barland, J. R. Tredicce, M. Brambilla, L. A. Lugiato, S. Balle, M. Giudici, T. Maggipinto, L. Spinelli, G. Tissoni, T. Knödl, M. Miller, and R. Jäger, Nature (London) **419**, 699 (2002).
[11] I. Favero and K. Karrai, Nat. Photonics **3**, 201 (2009).
[12] M. Aspelmeyer, T. J. Kippenberg, and F. Marquardt, Rev. Mod. Phys. **86**, 1391 (2014).
[13] J. Chan, T. P. Mayer Alegre, A. H. Safavi-Naeini, J. T. Hill, A. Krause, S. Gröblacher, M. Aspelmeyer, and O. Painter, Nature (London) **478**, 89 (2011).
[14] L. Ding, C. Baker, P. Senellart, A. Lemaître, S. Ducci, G. Leo, and I. Favero, Appl. Phys. Lett. **98**, 113108 (2011).
[15] C. Baker, W. Hease, D. T. Nguyen, A. Andronico, S. Ducci, G. Leo, and I. Favero, Opt. Express **22**, 14072 (2014).
[16] L. Ding, C. Baker, P. Senellart, A. Lemaître, S. Ducci, G. Leo, and I. Favero, Phys. Rev. Lett. **105**, 263903 (2010).
[17] L. Ding, C. Baker, A. Andronico, D. Parrain, P. Senellart, A. Lemaître, S. Ducci, G. Leo, and I. Favero, *Handbook of Optical Microcavities* (PanStanford, Singapore, 2014).
[18] A. Andronico, I. Favero, and G. Leo, Opt. Lett. **33**, 2026 (2008).

[19] P. S. Kuo, J. Bravo-Abad, and G. S. Solomon, Nat. Commun. **5**, 3109 (2014).
[20] S. Mariani, A. Andronico, A. Lemaître, I. Favero, S. Ducci, and G. Leo, Opt. Lett. **39**, 3062 (2014).
[21] I. Roland, A. Borne, M. Ravaro, R. De Oliveira, S. Suffit, P. Filloux, A. Lemaître, I. Favero, and G. Leo, Opt. Lett. **45**, 2878 (2020).
[22] D. Navarro-Urrios, N. E. Capuj, M. F. Colombano, P. D. Garcia, M. Sledzinska, F. Alzina, A. Griol, A. Martinez, and C. M. Sotomayor-Torres, Nat. Commun. **8**, 14965 (2017).
[23] J. Wu, S. W. Huang, Y. Huang, H. Zhou, J. Yang, J. M. Liu, M. Yu, G. Lo, D. L. Kwong, S. Duan, and C. W. Wong, Nat. Commun. **8**, 15570 (2017).
[24] T. Carmon, M. C. Cross, and K. J. Vahala, Phys. Rev. Lett. **98**, 167203 (2007).
[25] L. Ding, C. Belacel, S. Ducci, G. Leo, and I. Favero, Appl. Opt. **49**, 2441 (2010).
[26] C. Höhberger Metzger and K. Karrai, Nature (London) **432**, 1002 (2004).
[27] T. Carmon, H. Rokhsari, L. Yang, T. J. Kippenberg, and K. J. Vahala, Phys. Rev. Lett. **94**, 223902 (2005).
[28] F. Marquardt, J. G. E. Harris, and S. M. Girvin, Phys. Rev. Lett. **96**, 103901 (2006).
[29] C. Metzger, M. Ludwig, C. Neuenhahn, A. Ortlieb, I. Favero, K. Karrai, and F. Marquardt, Phys. Rev. Lett. **101**, 133903 (2008).
[30] B. Guha, S. Mariani, A. Lemaître, S. Combrié, G. Leo, and I. Favero, Opt. Express **25**, 24639 (2017).
[31] T. J. Johnson, M. Borselli, and O. Painter, Opt. Express **14**, 817 (2006).
[32] P. E. Barclay, K. Srinivasan, and O. Painter, Opt. Express **13**, 801 (2005).
[33] L. Ding, P. Senellart, A. Lemaître, S. Ducci, G. Leo, and I. Favero, Proc. SPIE Int. Soc. Opt. Eng. **7712**, 771211 (2010).
[34] I. Favero. Optomechanical interactions, *Quantum Optomechanics and Nanomechanics Lecture Notes of the Les Houches Summer School* (Oxford University Press, Oxford, England, 2020).
[35] B. Guha, P. E. Allain, A. Lemaître, G. Leo, and I. Favero, Phys. Rev. Applied **14**, 024079 (2020).
[36] D. Parrain, C. Baker, G. Wang, A. Lemaitre, P. Senellart, G. Leo, S. Ducci, and I. Favero, Opt. Express **23**, 19656 (2015).
[37] B. Guha, F. Marsault, F. Cadiz, L. Morgenroth, V. Ulin, V. Berkovitz, A. Lemaître, C. Gomez, A. Amo, S. Combrié, B. Gérard, G. Leo, and I. Favero, Optica **4**, 218 (2017).
[38] A. Baron, A. Ryasnyanskiy, N. Dubreuil, P. Delaye, Q. Vy Tran, S. Combrié, A. de Rossi, R. Frey, and G. Roosen, Opt. Express **17**, 552 (2009).
[39] Z. Zhou, C. Lu, S. Xu, Y. Jiang, B. Yun, C. Wang, and Y. Cui, Appl. Phys. Lett. **103**, 231111 (2013).
[40] See Supplemental Material at http://link.aps.org/supplemental/10.1103/PhysRevLett.126.243901. It contains two figures that display the generated mechanical comb spectrum, as well as the dynamics of the free-carrier density, temperature elevation, and intracavity photon number.
[41] A. A. Savchenkov, A. B. Matsko, V. S. Ilchenko, D. Seidel, and L. Maleki, Opt. Lett. **36**, 3338 (2011).
[42] A. Ganesan, C. Do, and A. Seshia, Phys. Rev. Lett. **118**, 033903 (2017).
[43] D. A. Czaplewski, C. Chen, D. Lopez, O. Shoshani, A. M. Eriksson, S. Strachan, and S. W. Shaw, Phys. Rev. Lett. **121**, 244302 (2018).
[44] L. Mercier de Lépinay, B. Pigeau, B. Besga, P. Vincent, P. Poncharal, and O. Arcizet, Nat. Nanotechnol. **12**, 156 (2017).
[45] S. Forstner, S. Prams, J. Knittel, E. D. van Ooijen, J. D. Swaim, G. I. Harris, A. Szorkovszky, W. P. Bowen, and H. Rubinsztein-Dunlop, Phys. Rev. Lett. **108**, 120801 (2012).
[46] J. Chae, S. An, G Ramer, V. Stavila, G. Holland, Y. Yoon, A. A. Talin, M. Allendorf, V. A Aksyuk, and A. Centrone, Nanoletters **17**, 5587 (2017).
[47] P. E. Allain, L. Schwab, C. Mismer, M. Gely, E. Mairiaux, M. Hermouet, B. Walter, G. Leo, S. Hentz, M. Faucher, G. Jourdan, B. Legrand, and I. Favero, Nanoscale **12**, 2939 (2020).
[48] D. Hälg, T. Gisler, Y. Tsaturyan, L. Catalini, U. Grob, M. D. Krass, M. Héritier, H. Mattiat, A. K. Thamm, R. Schirhagl, E. C. Langman, A. Schliesser, C. L. Degen, and A. Eichler, Phys. Rev. Applied **15**, L021001 (2021).
[49] W. Yu, W. C. Jiang, Q. Lin, and T. Lu, Nat. Commun. **7**, 12311 (2016).
[50] M. Sansa, M. Defoort, A. Brenac, M. Hermouet, L. Banniard, A. Fafin, M. Gely, C. Masselon, I. Favero, G. Jourdan, and S. Hentz, Nat. Commun. **11**, 3781 (2020).